Remote Sensing of Environment 268 (2022) 112759

Contents lists available at ScienceDirect

Remote Sensing of Environment

journal homepage: www.elsevier.com/locate/rse

Accuracy evaluation of digital elevation models derived from Terrestrial Radar Interferometer over Helheim Glacier, Greenland

Xianwei Wang [a,b,*], Denis Voytenko [c], David M. Holland [a,c]

[a] Center for Global Sea Level Change, New York University Abu Dhabi, Abu Dhabi 129188, United Arab Emirates
[b] School of Oceanography, Shanghai Jiao Tong University, Shanghai 200030, China
[c] Courant Institute of Mathematical Sciences, New York University, New York 10012, United States

ARTICLE INFO

Editor: Jing M. Chen

Keywords:
Helheim Glacier
Terrestrial radar interferometer
Digital elevation model
ICESat/GLAS
ICESat-2/ATLAS
ArcticDEM
Accuracy and precision

ABSTRACT

Glaciers in polar regions are sensitive to climate and ocean changes and can thin rapidly as a consequence of global warming. Digital Elevation Models (DEMs) from remote sensing observations have been widely used to detect changes in polar glaciers. DEMs from Terrestrial Radar Interferometer (TRI) have recently been used for high frequency glacier change and glacier-ocean interaction studies. However, it is unclear whether TRI DEM over a large study area can be combined directly with remote sensing observations to investigate glacier changes as well as the accuracy of TRI DEM at far range. In this study, we deployed a TRI close to Helheim Glacier, East Greenland and generated DEMs using TRI and satellite laser altimetry. We analyzed the accuracy of the TRI DEM using theoretical calculations, comparisons based on repeat observations, and comparisons with a high accurate ArcticDEM. The validation results suggest that for stable ground surfaces, the uncertainty (standard deviation) is <5 m at range < 9.8 km. Averaging across time (e.g. one hour) decreases the uncertainty almost linearly with range, over 0.5 m to 1.2 m when the range increases from 7.0 km to 10.0 km. Increasing the correlation coefficient threshold for phase unwrapping does not significantly reduce uncertainty. TRI DEMs are influenced by systematic error at far range primarily due to coarse azimuth resolution and phase unwrapping difficulties in discontinuous interferograms. As the absolute accuracy of TRI DEMs is not uniformly distributed in the range direction (farther points have worse uncertainty), our findings indicate that TRI DEMs within range of 10 km can reach <5 m uncertainty, which can be compared with DEMs obtained from remote sensing satellites to detect glacier thinning.

1. Introduction

The cryosphere of the Earth is changing rapidly due to global climate (Oppenheimer, 1998; Cox et al., 2000) and ocean changes (Holland et al., 2008) and as a consequence, glaciers in Greenland and Antarctica are melting and retreating (Rignot et al., 2011; Velicogna, 2009; Pritchard et al., 2012; Paolo et al., 2015; Shepherd et al., 2018; Joughin and Alley, 2011; Joughin et al., 2020; Smith et al., 2020) significantly. During the retreat of a glacier, the glacier thins gradually resulting in decrease of the ice thickness. Thus, one sign to tell whether a glacier is in retreat is to detect the thinning of the glacier (Howat et al., 2005; Kehrl et al., 2017). Since a glacier in thinning leads to decreased elevation, Digital Elevation Models (DEMs) obtained on different observation dates are usually required to detect glacier thinning.

Radar interferometry, such as the Shuttle Radar Topography Mission (SRTM) (Paul, 2008; Brown et al., 2005; Rodriguez et al., 2006), European Remote-Sensing Satellite (ERS)-1/2 (Sandwell and Sichoix, 2000), Environmental Satellite (Envisat) (Yu et al., 2014; Wegmüller et al., 2009), RADARSAT-1/2/Constellation (Gelautz et al., 2003), TerraSAR-X, TerraSAR-X add-on for Digital Elevation Measurements (TanDEM-X) (Rizzoli et al., 2017), COnstellation of small Satellites for the Mediterranean basin Observation (COSMO) (Nitti et al., 2013) have been used to generate DEMs when the coherence coefficient of land features between primary and secondary images remains high. SRTM provided a high-quality global DEM, but lacked good coverage over polar regions because it reached a maximum latitude of about 60°N. The recently released TanDEM-X global DEM (Zink et al., 2014) extended the global coverage to 85° N and the entire southern hemisphere. The other satellites mentioned above can be used to generate DEMs over polar ice sheets and glaciers by using primary and secondary images obtained

* Corresponding author.
E-mail address: wangxianwei0304@163.com (X. Wang).

https://doi.org/10.1016/j.rse.2021.112759
Received 11 October 2020; Received in revised form 20 September 2021; Accepted 16 October 2021

nearly from a similar same orbit and observation geometry (e.g., ERS-1/2, Envisat, RADARSAT-1/2, Constellation, and Sentinel-1A/B). Using two satellites from the same track shortens the revisit time and contributes to better coherence and topographic interferogram quality for DEM production. The accuracy of DEMs generated from SRTM and TanDEM-X can reach 7.6 m (Gorokhovich and Voustianiouk, 2006) and 2 m (Zink et al., 2014) at the global scale respectively.

Besides radar interferometry, spaceborne photogrammetry satellites have also been used to produce DEMs over polar ice sheets and glaciers, such as Advanced Spaceborne Thermal Emission and Reflection Radiometer (ASTER) (Tachikawa et al., 2011), Panchromatic Remote-sensing Instrument for Stereo Mapping (PRISM) onboard the Advanced Land Observing Satellite (ALOS) (Tadono et al., 2014), WorldView-1/2/3, GeoEye-1 (Howat et al., 2019; Noh and Howat, 2015) and SPOT 5 (Shean et al., 2019). Currently, freely-available continental-scale DEMs are primarily ASTER Global DEM (GDEM) (Tachikawa et al., 2011), ALOS Global Digital Surface Model (Tadono et al., 2014), the ArcticDEM (Porter et al., 2018), the Greenland Ice sheet Mapping Project (GIMP) (Howat et al., 2014), and the Reference Elevation Model of Antarctica (REMA) (Howat et al., 2019). Because visible or near infrared bands are usually used for acquisition of stereo images, clouds can degrade the DEM. Relatively larger errors or data gaps exist in the ASTER GDEM, especially close to coastal regions of ice sheets due to clouds (Wang et al., 2018). Similar to ASTER GDEM, the ALOS PRISM global DEM contains large data gaps over Antarctica, but has good coverage over the Greenland Ice Sheet, with an accuracy of around 5 m (Takaku et al., 2018). High resolution DEMs such as GIMP, REMA, and the ArcticDEM have relatively high accuracy, ± 24 m (when surface slope reaches 2°), ~ 1 m, and ~0.2 m (internal accuracy) respectively (Howat et al., 2014; Howat et al., 2019; Noh and Howat, 2015; Dai et al., 2018).

Another widely adopted method for DEM generation over polar glaciers uses radar and laser altimetry or light detection and ranging (Lidar), such as ERS-Radar Altimeter (RA), Envisat-RA2, Cryosat-2, the Geoscience Laser Altimeter System onboard the Ice, Cloud, and land Elevation Satellite (ICESat/GLAS) (Zwally et al., 2002; Fricker et al., 2005; Wang et al., 2011), ICESat-2/ Advanced Topographic Laser Altimeter System (ATLAS) (Smith et al., 2020), Ice-Bridge Airborne Topographic Mapper (ATM) (Krabill et al., 2002; Wang and Holland, 2018; Wang et al., 2018), Leica ALS50-II Airborne Laser Scanner from Natural Environment Research Council (NERC) Airborne Research & Survey Facility (ARSF) (Everett et al., 2021) and National Center for Airborne Laser Mapping (Telling et al., 2017). However, altimeters can only provide accurate point measurements along ground tracks with large data gaps between adjacent tracks, which are infilled using spatial interpolation. Because of the larger footprint of radar altimetry, its performance depends on surface slope. Laser altimetry or Lidar, however, such as ICESat/GLAS, ICESat-2/ATLAS and Ice-Bridge ATM can provide more accurate data for glacier change studies, ~15 cm (Zwally et al., 2002; Brunt et al., 2019; Smith et al., 2019; Krabill et al., 2002).

Although radar interferometry, photogrammetry and altimetry have provided high accuracy and long time-series data, they are not able to measure fast flowing outlet glaciers. The accuracy of coastal DEMs from photogrammetry is still a challenging problem (Wang et al., 2018) because of rapidly changing atmospheric conditions (e.g. clouds) and strong ocean-ice-atmosphere interactions. Altimetry relies on point measurements rather than plenary observations and leaves large DEM data gaps over coastal glaciers. Spaceborne sensors have long revisit time and can not satisfy the requirement of high frequency change studies such as interactions of tidewater glaciers with surrounding oceans, so some high frequency observations from a land-based instrument are required to fulfill this objective.

Recently, ground-based radar interferometer (Noferini et al., 2007; Pieraccini and Miccinesi, 2019), such as Terrestrial Radar Interferometer (TRI) has been developed (Werner et al., 2009) and deployed to detect rapid changes at coastal glaciers in Iceland (Dixon et al., 2012) and Greenland (Voytenko et al., 2015a, 2017; Holland et al., 2016; Cassotto et al., 2019, 2021). TRI is especially useful in Greenland for two reasons. First, most glaciers in Greenland terminate in a narrow and deep fjord and interact with surrounding oceans (Holland et al., 2016; Wood et al., 2021) at a high frequency. These rapid changes, such as ice calving, and ice mélange motion (Cassotto et al., 2015, 2021; Lüthi and Vieli, 2016; Peters et al., 2015; Walter et al., 2020; Xie et al., 2019) are not easy to detect by remote sensing satellites, but can be done through long-term TRI deployment. Second, TRI can provide dense and broad coverage (meter-scale pixels over 10 s of square km area) day and night with relative insensitivity to weather.

DEMs from radar interferometry, photogrammetry and laser and radar altimeters have played significant roles in polar glacier change studies because of their wide coverage, time saving and economy-efficient characteristics in data collection. TRI has also played a role in ice motion detection (Voytenko et al., 2015a, 2015b, 2017; Holland et al., 2016; Caduff et al., 2015; Cassotto et al., 2019) along with ice mélange changes (Xie et al., 2016, 2018, 2019; Cassotto et al., 2021) in Greenland. Long term TRI deployment may be combined with satellite or airborne observations to investigate glacier changes more efficiently. However, it is unclear whether DEMs from TRI can be directly compared with remote sensing observations because the accuracy of TRI DEMs over a large study area has not been fully validated although some works have been published by Strozzi et al. (2011), and Xie et al. (2019). Few researches have been conducted to study the consistency of TRI DEMs with satellite observations. Therefore, we investigate the accuracy of TRI DEMs over a large study area and how they are referenced to an ellipsoid surface, how they are impacted by interferometric correlation, how the systematic error can influence the final DEM generation, how averaging can improve the final quality of DEM, and how TRI DEM compared with other high resolution DEMs.

2. Data

2.1. Terrestrial radar interferometer (TRI) data

The Terrestrial Radar Interferometer (Fig. 1) used in this study was Gamma Portable Radar Interferometer-2 (GPRI-II), which was purchased from Gamma Remote Sensing (Hereafter, we use TRI to stand for this equipment). Our TRI is a real aperture and Frequency-Modulated Continuous-Wave (FMCW) radar interferometer (Werner et al., 2008, 2009), which can be operated on a ground platform to detect rapid land surface changes. Our TRI is also a Ku-band radar which operates at center frequency of ~17.2 GHz (Werner et al., 2009), with wavelength of ~1.74 cm (Werner et al., 2008, 2009; Strozzi et al., 2011; Voytenko et al., 2012, 2017) and can be operated during both day and night. The TRI is usually mounted on a solid pedestal (Fig. 1a) and can scan the ground surface from one side to another with a maximum scanning angle of 360 degrees. During operation, TRI illuminates the ground surface using one antenna mounted on top of radar frame and receives the backscattered radar echoes using another two antennas mounted on the lower part of radar frame (Fig. 1a). The three antennas are set parallel to each other horizontally and the two lower receiving antennas are spaced apart a 25 cm vertical baseline. This geometry of the receiving antennas allows us to simultaneously receive the returned signals and calculate the topographic phase to generate a DEM without time induced phase coherence loss and atmospheric phase delay (Werner et al., 2008, 2009).

TRI collects data records according to the travel time of the transmitted radar signal and the earlier returned signal is recorded first. For each scan, line observation in azimuth direction is recorded from near range to far range and observations from multiple azimuth lines construct one scanning image. Over Helheim Glacier, we used an 8 ms FMCW chirp to scan a range of ~16 km and to cover the most important terminus region. Focused TRI images have a polar projection where the range and azimuth resolution is not the same. A nominal range

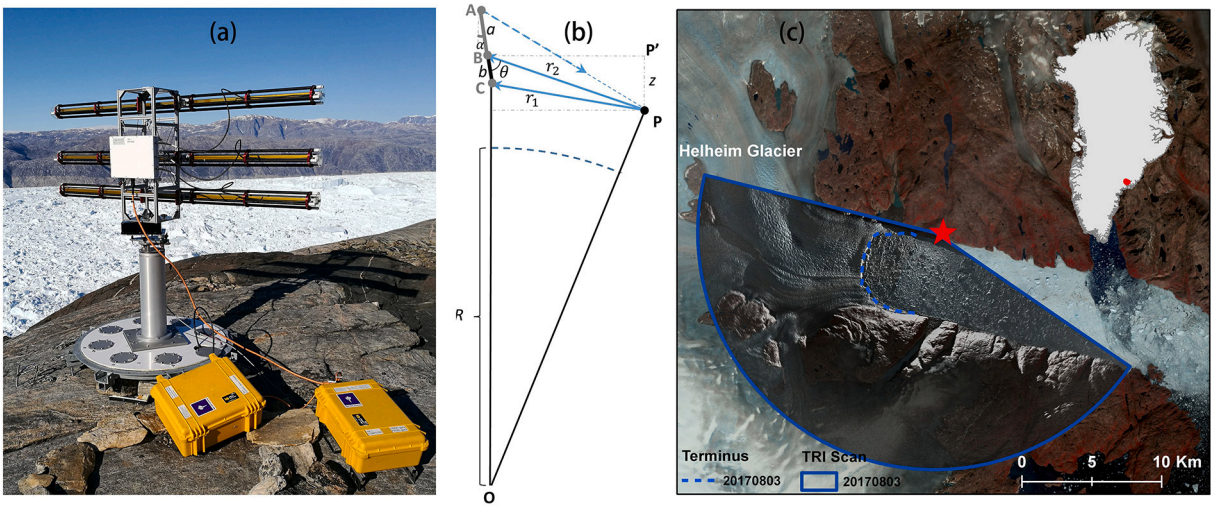

Fig. 1. (a) TRI setup close to Helheim Glacier, Greenland. One computer controlling the operation of TRI was stored in the lower right yellow pelican box. (b) Schematic map of the TRI observation geometry for ground surface observation. (c) The location of Helheim Glacier in East Greenland (red dot) and the TRI coverage over Helheim Glacier. An example TRI multi-looked image obtained on August 3, 2017 is shown in grayscale with 50% transparency overlaying an image from Sentinel-1. The location of TRI is marked with a solid red star. The extent of the TRI scan is outlined by a solid blue polygon and the calving front position on August 3, 2017 is indicated with a blue dashed line. This figure is plotted in UTM projection. (For interpretation of the references to colour in this figure legend, the reader is referred to the web version of this article.)

resolution of ~0.75 m (Werner et al., 2008, 2009) can be achieved while the azimuth resolution varies with the distance to the TRI (the azimuth resolution is determined by the physical antenna properties and range). The azimuth resolution along the slant range direction widens linearly with range distance (Werner et al., 2009; Strozzi et al., 2011; Voytenko et al., 2017): the closer it is to the TRI, the finer azimuth resolution. In our case, the azimuth resolution of our TRI at 1 km distance is about 7.5 m due to a nominal beam width (3 dB) of the transmitting antenna (Strozzi et al., 2011).

In this study, we deployed TRI near Helheim Glacier, East Greenland (Fig. 1) on August 3, 2017 and operated it continuously for one hour with a two-minute observation interval. A total number of 29 pairs of images from the upper and lower receiving antennas were obtained.

2.2. ICESat/GLAS data

The Ice, Cloud and land Elevation Satellite (ICESat) is the first spaceborne laser altimeter launched by NASA in 2003 with Geoscience Laser Altimeter System (GLAS) onboard (Zwally et al., 2002). Compared with traditional radar altimeters, ICESat/GLAS had smaller footprint, ~ 70 m in diameter on the ground. ICESat/GLAS transmitted continuous laser pulses at a wavelength of 1064 nm to measure the distance to the ground resulting in an accuracy of ~15 cm (Fricker et al., 2005; Shuman et al., 2006). Because of the high accuracy of altimetry data covering most ice sheets in Greenland and Antarctica, ICESat/GLAS data has been used to study changes in glacier elevation and ice mass balance (Pritchard et al., 2012; Wang et al., 2016, 2018). In this study, we use the ICESat/GLAS GLA12 data, which corresponds to ice sheet elevation

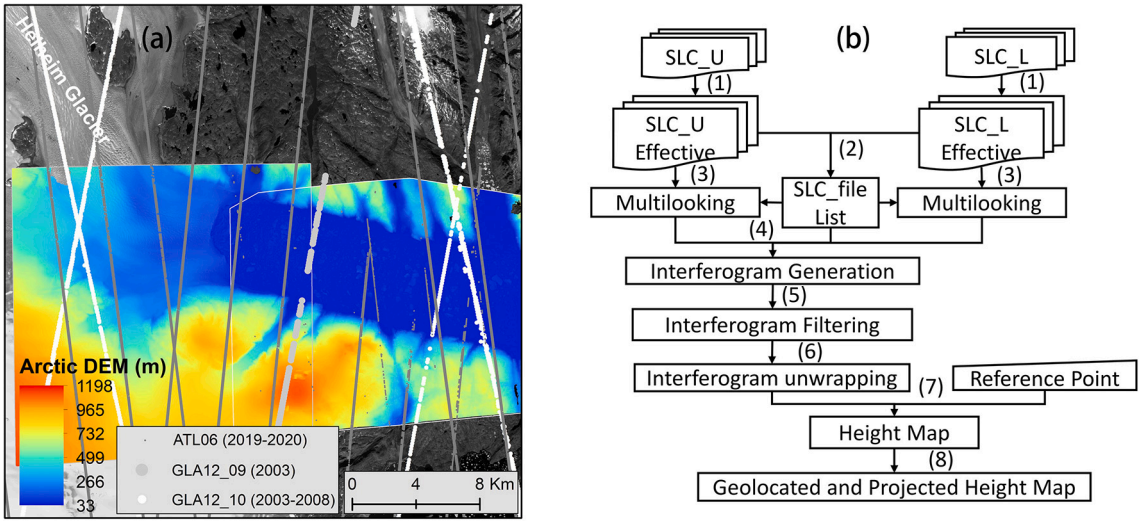

Fig. 2. (a) Two time-tagged stripes of ArcticDEM (images collected on July 1, 2017 and September 7, 2017 respectively) close to the TRI scanning period, ICESat/GLAS GLA12 data from September and October and ICESat-2 ATL 06 data from July to September 2019–2020 covering Helheim Glacier. GLA12_09 (2003) indicates the GLA12 data obtained from September 2003 and GLA12_10 (2003–2008) indicates the GLA12 data obtained from October 2003 to 2008. (b) Processing flowchart of TRI measurements. "SLC_U" and "SLC_L" indicate SLC measurements from the upper and lower receivers of TRI respectively. The indexes in brackets correspond to steps mentioned in Section 3.1.

collected in summer (from May to October), 2003 to 2009 (Fig. 2a) as reference points to control and evaluate the accuracy of TRI DEMs.

2.3. ICESat-2 data

The Ice, Cloud, and land Elevation Satellite-2 (ICESat-2) was launched on September 15, 2018 (Smith et al., 2019) with the Advanced Topographic Laser Altimeter System (ATLAS) as its primary sensing instrument. ICESat-2/ATLAS uses green laser light (532 nm) and photon-counting techniques to measure the surface elevation along tracks (Markus et al., 2017). Unlike ICESat/GLAS, which had only one single beam for land surface detection, ICESat-2/ATLAS has six beams (three pairs) providing high-density photon clouds for elevation measurement. In this study, we use ATL 06 data (land ice along-track data product) over Helheim Glacier (Fig. 2a) from July to September since 2018 to evaluate DEM accuracy because it averages elevation data along 40 m segments of ground track, spaced 20 m apart for six different beams with an accuracy better than 3 cm (Brunt et al., 2019).

2.4. Landsat ETM+ data

The Landsat 7 satellite used the Enhanced Thematic Mapper Plus (ETM+) as the primary optical sensor (Goward et al., 2001) relying on eight band measurements to study changes in polar regions, land use and land cover classifications (Choi and Bindschadler, 2004; Crawford et al., 2013). The green and near infrared (NIR) bands corresponding to wavelengths of 0.52–0.60 μm and 1.55–1.75 μm respectively are usually combined to identify snow and ice and rock outcrops (Hui et al., 2013). In this study, rock outcrops around Helheim Glacier are classified using one Landsat ETM+ image (Supplementary Table 1) obtained in July of 2002. Because of atmospheric warming and rapid retreat of Helheim Glacier, some rock outcrops covered by snow and ice before 2003 (the start time of laser altimetry measurements used in this study) may have become exposed later. Thus, the rock outcrops extracted from summer 2002 can be considered unchanged, and with consistent elevation since 2003.

2.5. ArcticDEM data

The ArcticDEM (Porter et al., 2018) is generated by applying stereo auto-correlation techniques (Noh and Howat, 2015) to overlapping pairs of high-resolution Geoeye-1, WorldView-1, WorldView-2, and WorldView-3 images (Howat et al., 2019). The ArcticDEM project currently has ~260,000 total timestamped DEMs (Porter et al., 2018) with a spatial resolution of 2-m covering all Arctic, land area north of 60° (Porter et al., 2018). In this study, we use ArcticDEM data covering Helheim Glacier (Supplementary Table 1) obtained around summer 2017 (Fig. 2a) to evaluate the accuracy of our TRI DEMs.

3. DEM production and rectification from TRI observations

In this section, we first introduce referencing TRI DEMs to an ellipsoid surface. Second, we extract rock outcrops in the study from Landsat images. Finally, we use laser altimetry data from ICESat/GLAS over rock outcrops to correct the TRI DEM assuming the elevation of rock outcrops does not change with time. In this study, rock outcrops over Helheim Glacier are considered as possible reference points, which have consistent land elevation over time for the same region. Although the land surface is changing due to elastic change and postglacial rebounding (Khan et al., 2020), the small amount of change from 2003 to 2020 is not considered (Section 3.2). The details of each step in this section are introduced as follows.

3.1. DEM generation using TRI observations

DEM generation using interferometry has been widely used, especially for spaceborne or airborne observations (Zebker and Goldstein, 1986. Dall et al., 2001) and similar data processing techniques have also been adopted for TRI data. Our TRI was deployed around Helheim Glacier, East Greenland with the observation geometry shown in Fig. 1a and b. According to topography height generation theory from interferometry and following Zebker and Goldstein (1986), Strozzi et al. (2011), Eqs. (1) to (4) can be obtained.

$$\begin{cases} r_1^2 = b^2 + r_2^2 - 2br_2 cos\theta \ (1) \\ cos(\theta + \alpha) = \dfrac{z}{r_2} \ (2) \\ \varnothing = -\dfrac{2\pi}{\lambda}(r_1 - r_2) \ (3) \\ \alpha \ll \theta \ (4) \end{cases}$$

where point A, B, C, O, and P corresponds to location of transmitter, upper receiver, lower receiver of TRI, the center of the Earth and ground surface point. P′ is the vertical projection of P in horizontal plan which passes through B. a, b, r_1, r_2, R and z corresponds to distance from A to B, baseline (distance from B to C), distance from P to C, distance from P to B, the radius of the Earth, and the vertical height difference of P with B. α and θ are the baseline angle and look angle (the symbols can be found from Fig. 1b). $\varnothing$ is the topographic phase generated from path difference of r_1 and r_2. Then the height difference (z) of P with B can be solved by following Strozzi et al. (2011) as

$$z = \frac{\lambda r_2 \varnothing}{2\pi b} + \frac{b}{2} - \frac{\lambda^2 \varnothing^2}{8\pi^2 b} \quad (5)$$

z is the height difference assuming a flat Earth.

The processing steps corresponding to Eqs. (1) to (5) using GAMMA software are introduced as follows. The flowchart corresponds to this processing can be found from Fig. 2b.

(1) The SLC (Single Look Complex) data obtained from TRI are checked first to make sure that no bad data are used for DEM generation. Sometimes the TRI could not correctly record the observed data, resulting in an empty or incomplete SLC data file. Those empty or incomplete files, which usually have different file sizes, should be deleted.
(2) Generate the file list of SLC data for interferometric processing using all available files from the upper and lower receiving antennas. The total number of image pairs is counted for the input of the next step.
(3) Generate multi-looked images for all SLC observation data. In this step, we average by a factor of 12 in range and 1 in azimuth. As the range resolution of TRI is relatively high, we multi-look more range samples in this process. This multi-looking process helps to reduce the noise level of the TRI images and the factor 12:1 can make pixels in multi-looked image squarer.
(4) Generate the Interferometric phase using all SLC data pairs. To improve the quality of the interferogram, the averaging parameters from (3) are used.
(5) Filter the interferogram using an adaptive filter (Goldstein and Werner, 1998). In this process, the window size of the filter is set to be 32 pixels to smooth the interferogram, and to improve the quality of topographic fringes to facilitate phase unwrapping.
(6) Unwrap the smoothed phase generated in step 5 with a minimum cost flow algorithm (Werner et al., 2002) and calculate the absolute phase difference for DEM generation. In this step, only phase measurements with an interferometric correlation coefficient lager than 0.7 (the setting of 0.7 can refer Section 5.5) are unwrapped to improve the quality of the final DEM.
(7) Generate the height map using the unwrapped phase and one reference location in the imaged area. The reference location is

usually chosen as rock outcrop, which does not move over time. In this step, pixel (715, 377) (715 in range and 377 in azimuth direction, solid black dot in Fig. 3b) corresponds to a rock outcrop and the reference elevation is set as zero. Thus, a height map is generated, but it is biased because no absolute elevation of the reference point is used.

(8) Geolocate the height map. Since the height map is in polar coordinates and can not be geolocated directly. It is reprojected to rectangular (planar) coordinates with a specified 10-m resolution. The height map is then rotated around the TRI location with the best offset angle, which is determined via comparisons with a georeferenced Landsat image from Section 2.3. (Some results during interferometric processing are shown in Fig. 3, which has been georeferenced and plotted in planar projection.)

In order to put the calculated height into some commonly used elevation system, such as WGS-84, an ellipsoid surface height correction is required. When the TRI scan range is small (less than 2 km), the ellipsoid height correction is negligible. However, when the scan range is large (greater than 10 km), the height correction caused by flat plane and ellipsoid surface can be larger than 10 m. Fig. 1b and Supplementary Fig. 1 show that the farther the range, the greater the correction. Thus, applying a height correction to ellipsoid surface to TRI DEMs is essential to guarantee the directional comparison with other DEMs generated with photogrammetry or altimetry.

$$\begin{cases} \bar{r} = r_2 sin(\theta+\alpha) \ (6) \\ E_p = E_A - a - r_2 cos(\theta+\alpha) \ (7) \\ \varphi = \text{atan}\left(\dfrac{\bar{r}}{E_p}\right) \ (8) \\ \Delta H = \dfrac{E_p+R}{cos\varphi} - (E_p+R) \ (9) \\ Z = z + \Delta H \ (10) \end{cases}$$

Where E_A is the ellipsoidal height of point A, determined by a GPS receiver (WGS-84 ellipsoid height) directly, R is the ellipsoidal radius of the Earth, $\bar{r}$ is the ground range from TRI to the illuminated region which can be obtained during processing (introduced in the remainder of this section) directly, E_p is the elevation of point p, ΔH is the ellipsoidal height correction and Z is the ellipsoid height.

As the range and elevation variation from TRI is far smaller than the

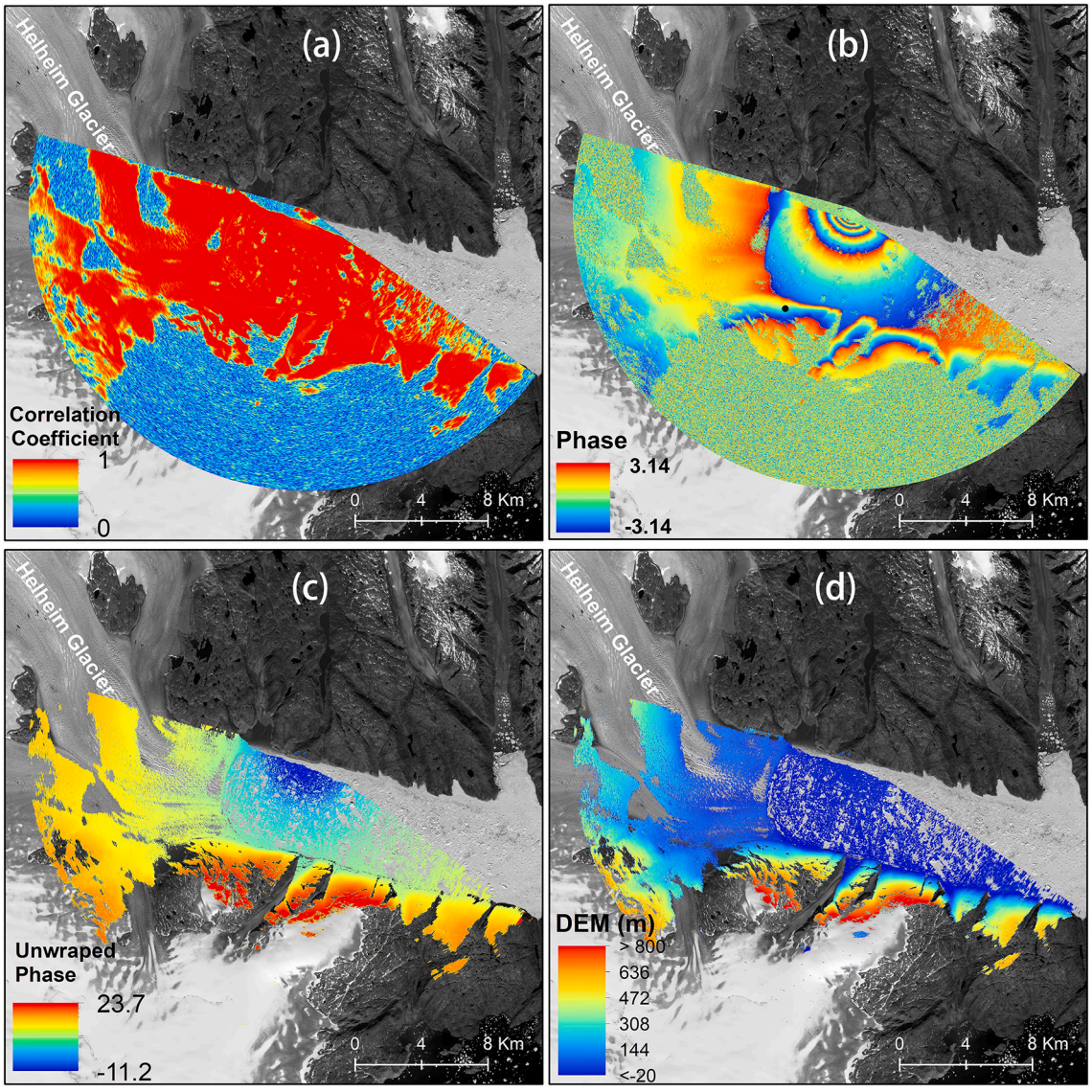

Fig. 3. (a) Correlation coefficient between SLC images from the upper and lower antennas of the TRI. (b) Interferometric (wrapped) phase from TRI processing. The solid black dot indicates the reference point for phase unwrapping (c) Unwrapped phase for DEM generation. (d) DEM from TRI processing (no elevation reference).

radius of the Earth, a simple WGS-84 ellipsoid height correction is applied using the range obtained in the step (8) assuming no terrain variation (Supplementary Fig. 1).

3.2. Rock outcrops classification

Rock outcrops around Helheim Glacier can be considered to be stable land cover with no significant elevation change during the observation periods between 2003 and 2020. Although the elevation changes because of elastic rebound and glacial isostatic adjustment (Khan et al., 2020) can reach ~13 cm, this small-scale elevation change is not considered because the rock surface around Helheim Glacier is rough and the elevation change is beyond the detection capability of laser altimetry. Thus, the elevation of rock outcrops can be compared between different DEMs to evaluate the accuracy of DEMs. Rock outcrops, snow and ice are the primary land covers around Helheim Glacier. In order to identify rock outcrops from snow and ice, the Normalized Difference Snow Index (NDSI) is usually used (Dozier, 1989; Burton-Johnson et al., 2016). In this study, we analyze Landsat ETM+ data obtained from July 2002 and calculate NDSI Eq. (11)

$$NDSI = \frac{B2 - B5}{B2 + B5} \tag{11}$$

where *B2* and *B5* indicate the digital number of the green band and near infrared band (NIR) of Landsat ETM+ images corresponding to wavelengths of 0.52–0.60 μm and 1.55–1.75 μm, respectively.

Since the reflection of snow and ice from the visible band (*B*2) is higher than that from the near infrared band (*B*5) and the reflection of rock outcrops from *B*2 is lower than that from *B*5 (Dozier, 1989; Burton-Johnson et al., 2016), rock outcrops can be classified by analyzing the difference of NDSI from snow and ice. The NDSI over Helheim Glacier is calculated and shown in Fig. 4a and the histogram of NDSI is shown in Fig. 4b. The rock outcrops are shown in Fig. 4a, which is primarily indicated with blue colour. Since two primary land covers occurs around Helheim Glacier, rock outcrops are extracted by finding regions with NDSI lower than −0.2 (strict control which may exclude some rock outcrops).

3.3. DEM rectification

ICESat/GLAS GLA12 data have an elevation accuracy of ~15 cm and is a good elevation reference to correct the relatively rectified TRI DEMs to the WGS-84 ellipsoid. In this study, ICESat/GLAS GLA12 data collected in September 2003 from rock outcrops around Helheim Glacier is used to rectify the TRI DEMs. The ICESat/GLAS GLA12 elevation data is rectified to WGS-84 ellipsoid first by following Eq. (12) (Wang et al., 2013; E et al., 2007).

$$H_G = H_g - cos^2\varphi d_a - sin^2\varphi d_b \tag{12}$$

where H_G and H_g are the elevations directly read from the GLA12 data file referenced to WGS-84 and Topex/Poseidon ellipsoids respectively, φ the latitude of laser footprint, d_a and d_b the difference in semi-major and semi-minor axis of WGS-84 and Topex/Poseidon ellipsoids respectively.

The corrected ICESat/GLAS data are then used to correct the ArcticDEM and the TRI DEMs.

(1) We use the corrected ICESat/GLAS data over rock outcrops in summer 2003 and correct the two stripes of ArcticDEM by removing the height bias between them and mosaicking. The corrected ArcticDEM is then used to validate TRI DEMs.
(2) Because only one reference point from stable rock area is taken to generate TRI DEMs in Section 3.1 and no absolute elevation data from the reference point is used, the TRI DEMs are not correctly referenced. In order to rectify these DEMs, ICESat/GLAS data illuminating rock outcrops around Helheim Glacier from September and October 2003 are taken as references. In this way, the TRI DEMs are referred to the WGS-84 ellipsoid and can be compared with a DEM generated with stereo photogrammetry. The DEM derived from TRI data processing is then similarly rectified to WGS-84 ellipsoid by considering the elevation difference between each other, which can be implemented by following Eq. (13)

$$E = H + \Delta E \tag{13}$$

where *E* is the final corrected DEM from TRI, *H* is the original TRI DEM,

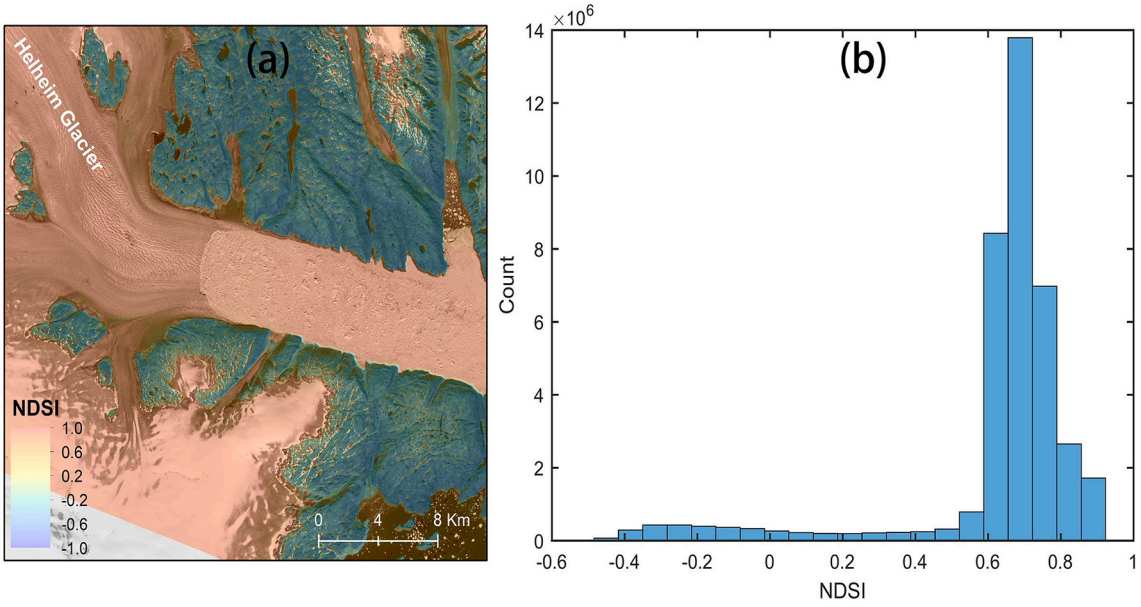

Fig. 4. (a) NDSI calculated from Landsat ETM+ data (Supplementary Table 1), which was captured on the 217th day of 2002. This image from 2002 is used to obtain the rock outcrops, which should have stable elevation over time. The NDSI data is overlain on a Sentinel-2 image captured on August 5, 2017. (b) Histogram of NDSI for the Landsat ETM+ image. Two primary land covers, snow/ice and rock outcrops can be seen from two peaks (one around 0.7, the other around −0.2) in the NDSI histogram.

and ΔE is the elevation difference between ICESat/GLAS GLA12 data and the original TRI DEM over rock outcrops.

4. Precision and accuracy of DEMs

4.1. Accuracy of ArcticDEM

The ArcticDEM is rectified using ICESat/GLAS data obtained in September 2003 and is validated using other ICESat/GLAS measurements obtained in October from 2003 to 2009 along with ICESat-2/ATLAS data from July to September since 2018. Elevation difference from 124 footprints and 3322 points is obtained from ICESat/GLAS and ICESat-2/ATLAS respectively, the spatial distribution of which are shown in Fig. 5a and c. The results show no obvious trend of the spatial distribution of elevation difference. The histograms of elevation difference shown in Fig. 5b and d indicate the mean of elevation difference ~ 0.4 m (standard deviation ~4.1 m) and ~ 0.3 m (standard deviation ~2.3 m) for ICESat/GLAS and ICESat-2/ATLAS respectively. The elevation difference follows a normal distribution, passing a z-test ($h = 0$, $p = 0.98$ and $h = 0$, $p = 0.93$ for ICESat/GLAS and ICESat-2/ATLAS validation respectively) at the default 5% significance level. These comparison results indicate that the accuracy of the corrected ArcticDEM is high and sufficient to quantify the accuracy of TRI DEMs.

4.2. Precision of TRI DEMs

To detect the precision of TRI DEMs, indicating their stability over the same ground surface across repeated measurements, we generate five DEMs over Helheim Glacier generated during a 10-min interval on August 3, 2017 (scanning interval 2 min). Considering the elevation of land cover did not change during this period, we calculate the mean and standard deviation of each pixel over the entire TRI DEM. As Helheim Glacier moved at ~24 m/d (Voytenko et al., 2015a, 2015b) close to the ice front, repeat measurements over a short time period can be compared assuming no calving. Here we choose 10 min of observation suggesting that the glacier motion was less than 20 cm, which is relatively small compared to the pixel resolution. Additionally, since no calving events occurred in that time period, the elevation variation is negligible. We produce an averaged DEM (Fig. 6a) using five SLC image pairs obtained over 10 min along with the standard deviation of elevation (Fig. 6b). Fig. 6b indicates that the elevation measurement at near range is more precise due to smaller standard deviation (indicated in

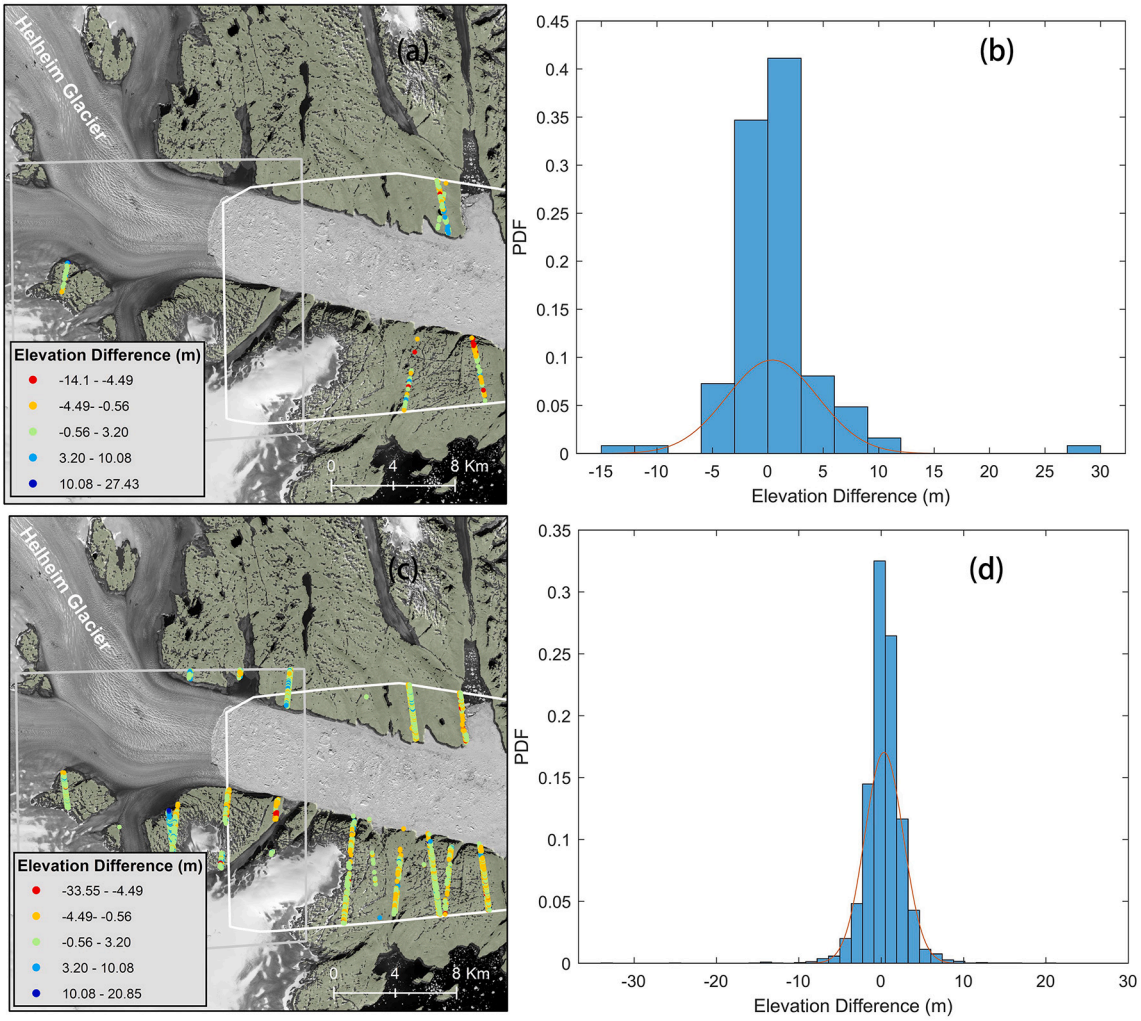

Fig. 5. Elevation differences of ICESat/GLAS and ICESat-2/ATLAS with ArcticDEM data. (a) and (c) indicate the spatial distribution of elevation difference of ICESat/GLAS and ICESat-2/ATLAS data over Helheim Glacier respectively. The shaded region indicates rock outcrops extracted using the NDSI threshold. The white polygons indicate the boundary of ArcticDEM, which is shown in Fig. 2. (b) and (d) indicate the statistics of elevation difference of ArcticDEM with ICESat/GLAS and ICESat-2/ATLAS respectively, both of which follow a normal distribution. Red curve indicates a normal distribution used for the significance test. Label 'PDF' in (b) and (d) is short for "Probability Density Function". (For interpretation of the references to colour in this figure legend, the reader is referred to the web version of this article.)

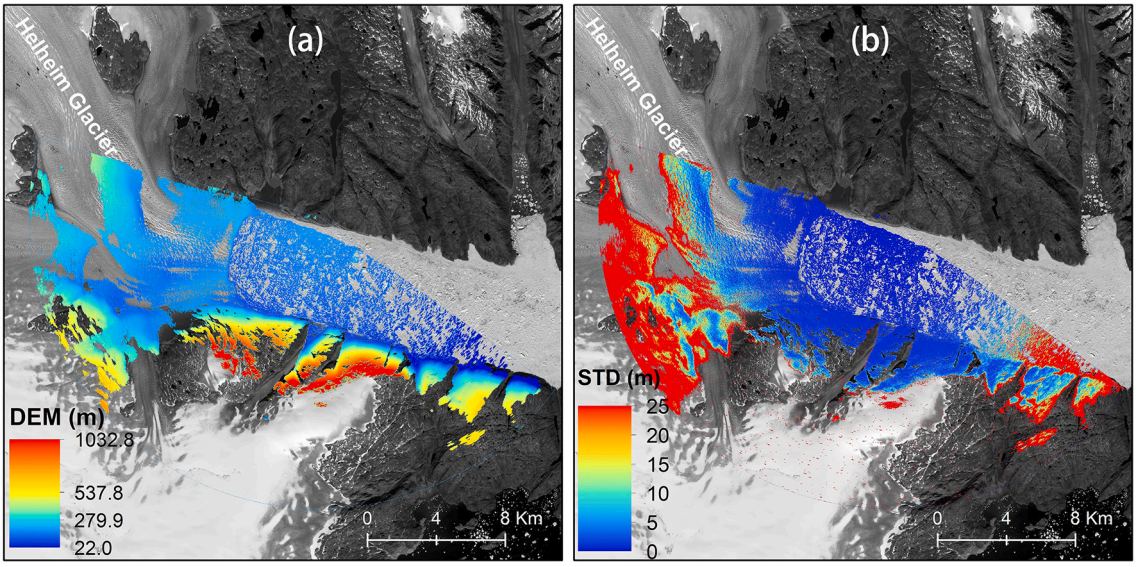

Fig. 6. (a) Digital Elevation Model (DEM) over Helheim Glacier, Greenland after correction with ICESat/GLAS data (only elevations with standard deviation <5 m are shown). (b) Pixel-level DEM elevation standard deviation using 10 min of TRI measurements (five TRI DEMs).

blue). However, at far range, the precision is poor, with standard deviation larger than several tens of meters (indicated in red).

4.3. Absolute accuracy of TRI DEM

Since the TRI DEM has been corrected using ICESat/GLAS data in Section 3.3, for further analysis, it is compared with the corrected ArcticDEM by calculating the elevation difference over the rock outcrops between both. Fig. 7a shows the spatial distribution of elevation difference obtained by subtracting ArcticDEM from the corrected TRI DEM. The absolute accuracy of TRI DEM is not uniformly distributed across the study area. The histogram of elevation difference shown in Fig. 7b indicates that the TRI DEM tends to be lower than the real value with mean elevation difference of ~ -58.6 m. The distribution of elevation difference with range is shown in Fig. 7c, which suggests that in our study area, the TRI DEM tends to provide lower elevation linearly with range increases. The absolute elevation difference can reach hundreds of meters at far range, which indicates that the absolute accuracy of TRI DEM is poor at far range when selecting only one ground control point. This result suggests it may be problematic to compare TRI DEM directly with other source DEMs at far range (Section 5.1), especially when trying to calculate the elevation change of a glacier due to climate change.

5. Discussion on TRI DEM

Since the TRI DEM is extracted after multiple processing steps (Section 3.1), such as multi-looking, interferometric correlation calculation, phase unwrapping, and elevation inversion, the accuracy of the final DEM can be influenced by many factors. In this section, we will discuss the influence of the correlation coefficient and slant range on the final accuracy of TRI DEM, systematic and other errors that can influence the final DEM accuracy, as well as how averaging can improve the final quality of TRI DEM. To better illustrate these questions, the TRI DEM is shown in radar (polar) coordinates. One TRI DEM is drawn in polar projection, along with the standard deviation, mean correlation coefficient and the standard deviation of correlation coefficient of the averaged TRI DEM (Fig. 8). Here only five pairs of TRI DEMs are used to calculate standard deviation for each pixel in Fig. 8. However, the difference of standard deviation when using 5 or 29 TRI DEM pairs is not

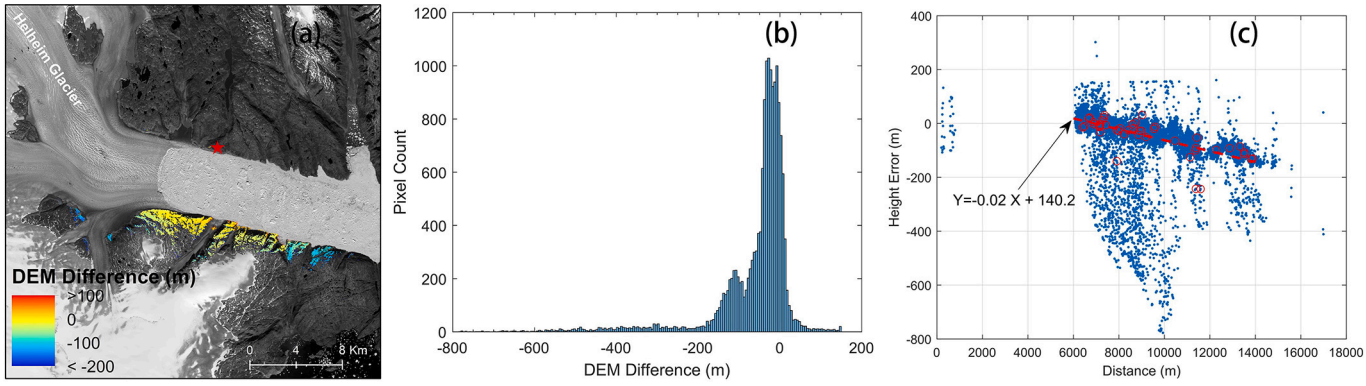

Fig. 7. DEM difference calculated by subtracting the corrected ArcticDEM from the corrected TRI DEM. (a) shows the spatial distribution of DEM difference over rock outcrops over Helheim Glacier. Similar to Fig. 1c, the location of TRI is indicated with a solid red star. (b) shows the histogram of DEM difference, the majority (92.3%) of DEM difference, is located in [−180, 60] meters. (c) shows the distribution of DEM difference with range and a linear trend of DEM difference is shown. Red dots indicate the pixels with same elevation of TRI, which is discussed in Sections 5.5 and 5.6. The linear trend of height error (Y) with distance (X) is fitted using the red dots, with the least square regression method and the fitted equation is shown in a dashed red line. (For interpretation of the references to colour in this figure legend, the reader is referred to the web version of this article.)

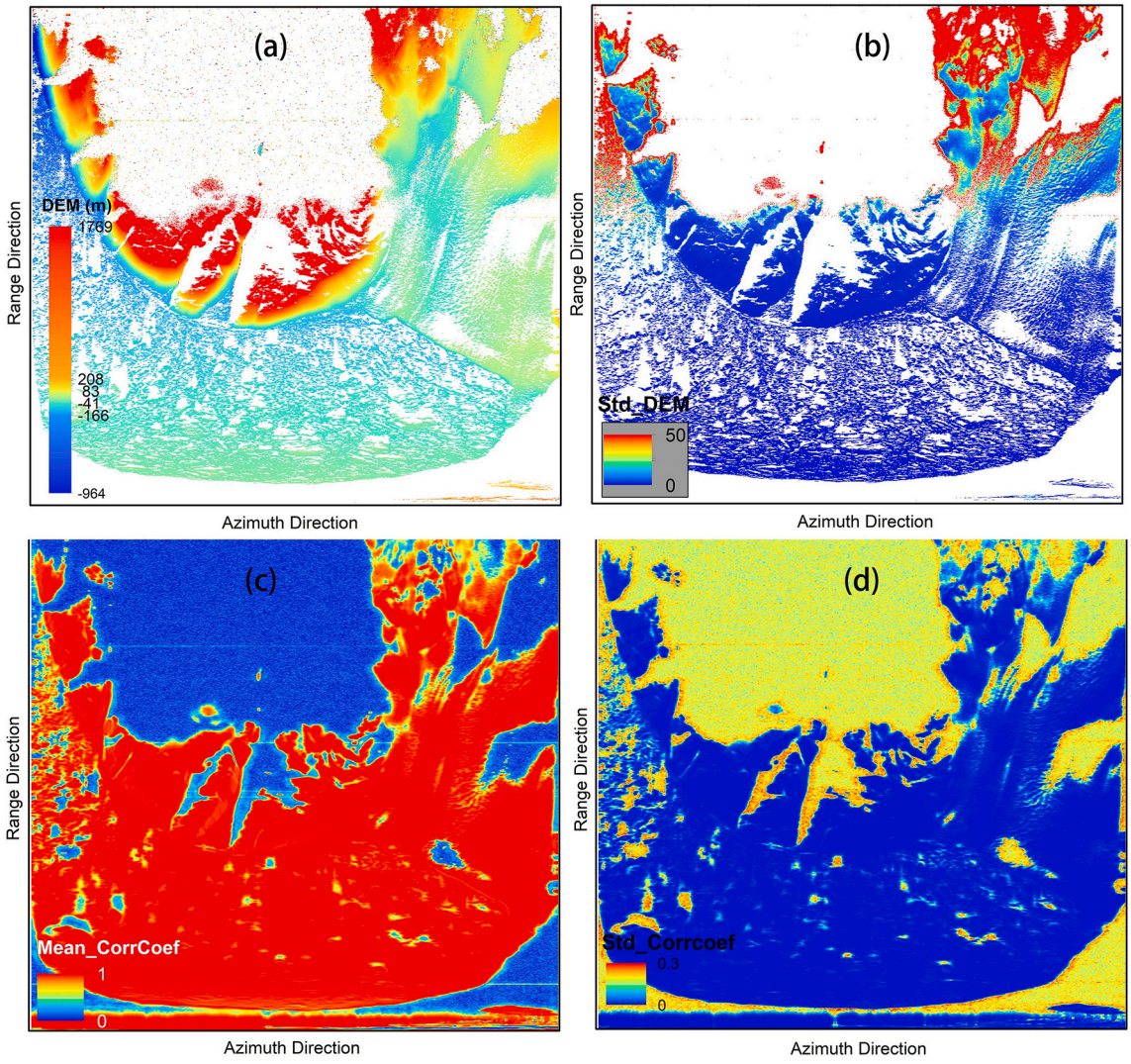

Fig. 8. (a) Mean DEM of Helheim Glacier derived from TRI observations. (b) Standard deviation of DEM over Helheim Glacier. (c) Mean of interferometric correlation coefficient before generating the TRI DEM. (d) Standard deviation of interferometric correlation. The horizontal direction indicates the scanning direction of TRI, from the left to the right (azimuth direction) and the vertical direction indicates the range direction, which increases from the bottom (near range) to the top (far range) in each subfigure.

significant (Supplementary Fig. 2), which indicates the standard deviation can be reflected properly.

5.1. Relation of DEM uncertainty with range

TRI scanned Helheim Glacier from one side to the other, the total time of which was ~32 s. Thus, the entire region of Helheim Glacier was not observed exactly at the same time. However, for each scan, the samples along range direction were recorded almost at the same time and the backscattered signals from glacier or rock were recorded from the near range to the far range.

Over our study area (Fig. 8a), there are 795 azimuth lines and 1868 range samples after the multi-looking process. Five two-minute DEMs are generated to investigate spatiotemporal variability. The mean standard deviation of TRI DEM, which corresponds to the mean of all available standard deviations at specific range is calculated across ranges (sample 1 to sample 1868) and is shown with in dots in Fig. 9a. The total number of effective azimuth line observations at that range is calculated as well, indicated by red dots in Fig. 9a.

From Figs. 8b and 9a, the standard deviation of TRI DEM increases with range, which has been pointed out in in Section 4.2. The distribution of the mean standard deviation of TRI DEM with range follows an exponential distribution (Eq. (14)) when the range sample is less than 1150 (equivalent to 11.5 km as range resolution is 10 m). However, when the range is greater than 11.5 km, the mean standard deviation of DEM is usually larger than 40 m and shows an increasing trend.

$$y = 0.01298e^{1.356\times10^{-6}x} \tag{14}$$

where x stands for range in meter and y stands for the mean standard deviation of DEM along range direction.

This exponential distribution (Eq. (14)) indicates that if we want to have a DEM with standard deviation <5 m, it is better to use only DEM data within 987 samples of ranges (equivalent to 9870 m).

5.2. Relation of DEM uncertainty with surface elevation

The topographic fluctuation over Helheim Glacier imaged by our TRI is about 1000 m. Fig. 8a, and b show that there is no relationship between the accuracy of TRI DEM and elevation at our site. We determine that there is no linear correlation between the elevation and the standard deviation of TRI DEM by calculating a correlation coefficient of $r = 0.16$ ($p < 0.05$) (the second column of Table 1). Similarly, interferometric correlation between signals from the upper and lower receiving

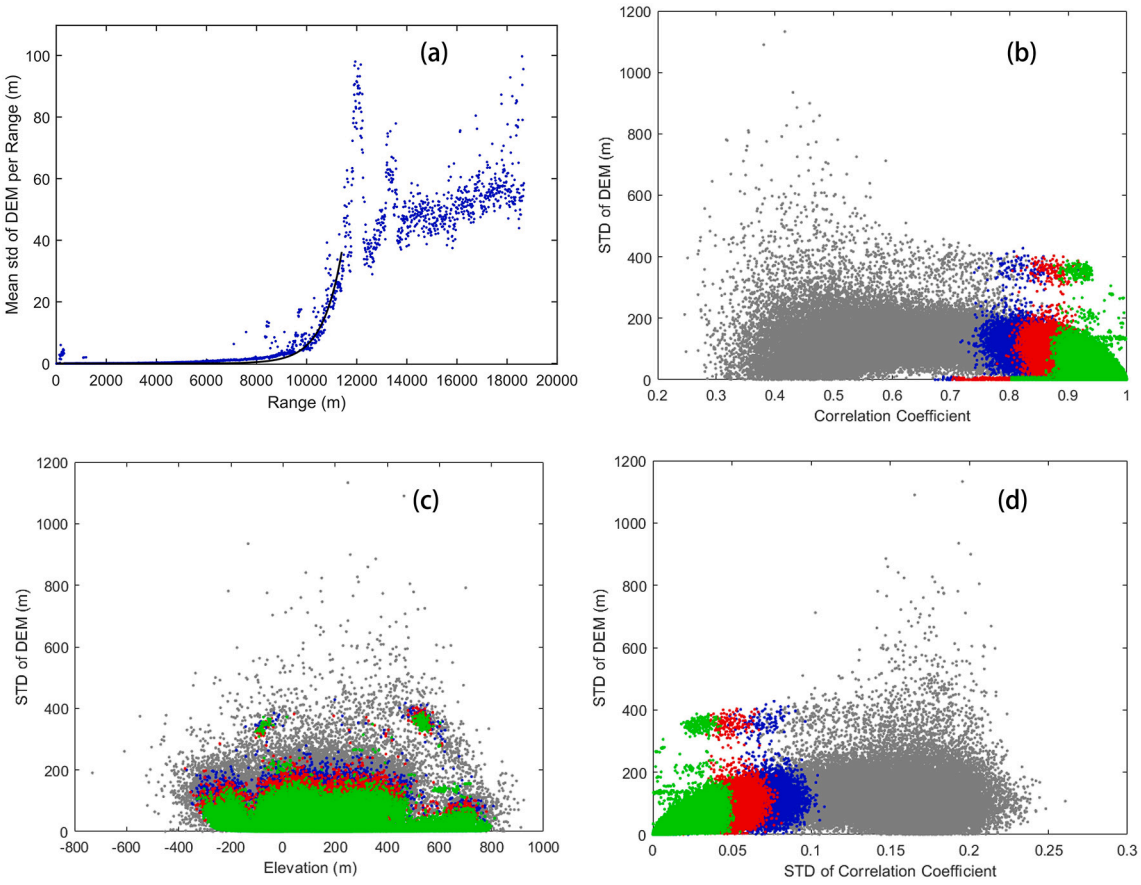

Fig. 9. (a) The left axis corresponds to the relation of standard deviation of TRI DEM with range. The black curve shows the fitted exponential distribution which is shown in Eq. (14), Section 5.1. (b), (c) and (d) show the relation of correlation coefficient, land surface elevation and standard deviation of correlation coefficient with standard deviation of the TRI DEM over Helheim Glacier respectively. The gray, blue, red and green points indicate pixels with interferometric correlation coefficient between, 0–0.6, 0.6–0.7, 0.7–0.8, 0.8–1.0 respectively. The density of land surface and different interferometric correlation coefficient can be found from Table 1. (For interpretation of the references to colour in this figure legend, the reader is referred to the web version of this article.)

Table 1
Count of effective pixels generated under different threshold of interferometric correlation and the relationship between elevation, interferometric correlation, and standard deviation of interferometric correlation with standard deviation of DEM. CC stands for the interferometric correlation. DEM_STD and CC_STD indicate the standard deviation of DEM and the standard deviation of interferometric correlation respectively.

Conditions of Pixel Selection	Elevation and DEM_STD	CC and DEM_STD	CC_STD and DEM_STD	Number of Effective Pixels
cc > 0	0.155 ($p < 0.05$)	−0.768 ($p < 0.05$)	0.798 ($p < 0.05$)	607,302
cc > 0.6	0.132 ($p < 0.05$)	−0.805 ($p < 0.05$)	0.852 ($p < 0.05$)	557,602
cc > 0.7	0.129 ($p < 0.05$)	−0.761 ($p < 0.05$)	0.842 ($p < 0.05$)	548,096
cc > 0.8	0.125 ($p < 0.05$)	−0.688 ($p < 0.05$)	0.823 ($p < 0.05$)	535,869

antennas suggests the same thing in Fig. 9c and Table 1This statistical analysis indicates that the final accuracy of TRI DEM may not be linearly related to topographic variations.

5.3. Relationship between DEM uncertainty and interferometric correlation

To generate low noise topographic phase for DEM production, a high interferometric correlation between SLC signals received from the upper and lower receiving antennas of TRI is required. Thus, the correlation of backscattered SLC signals is related to the final accuracy of TRI DEM. The mean interferometric correlation for all TRI image pairs is shown in Fig. 8c. Table 1 and Fig. 9b show the relationship between DEM uncertainty and interferometric correlation of SLC signals from the two receiving antennas.

Comparing Fig. 8b, c, and the statistical results in Table 1, we observe a negative linear correlation between DEM uncertainty (standard deviation of DEM) and interferometric correlation. This indicates that pixels with high interferometric correlation usually correspond to high accuracy of DEM pixels. However, the third column (CC and DEM_STD) of Table 1 does not increase with interferometric correlation, which indicates that a higher threshold setting of interferometric correlation during phase unwrapping may not always correspond to a more accurate DEM.

Fig. 9b also shows that the maximum standard deviation of TRI DEM decreased from more than 1000 m to about 390 m when increasing the threshold of interferometric correlation from 0 to 0.8. This suggests that increasing the threshold of interferometric correlation can dramatically decrease the maximum standard deviation of TRI DEM (gray, blue, red and green dots). This may be caused by smoother gradients during phase unwrapping. However, the result also reflects that a higher threshold setting change (from 0.60 to 0.80) may not significantly exclude elevation pixels with large uncertainty, as pixels with standard deviation of TRI DEM larger than 50 m still persist.

5.4. Relationship between DEM uncertainty and variation of interferometric correlation

By comparing Fig. 8c, d and Table 1, we can find that the interferometric correlation is negatively correlated with its standard deviation. This is because the backscattered radar echoes from the higher correlated land surface did not change over the observation period (an hour) and maintained high coherence. However, signals from the lower coherence regions, such as water surface, radar shadow areas were random and more variable, resulting in higher standard deviation.

The correlation statistics of TRI DEM accuracy with standard deviation of interferometric correlation are shown in the fourth column (CC_STD and DEM_STD) of Table 1. The results indicate that pixels with higher interferometric correlation (threshold setting in Table 1) corresponding to lower standard deviation of interferometric correlation (Fig. 9d), but the largest standard deviation of DEM does not change much when increasing threshold from 0.6 to 0.8.

Our analysis indicates that a high interferometric correlation threshold setting can reduce the standard deviation of the TRI DEM. However, it does not mean the larger settings are always better. This is because highly correlated backscatters, such as rock and ice are distributed discontinuously in space (Figs. 9b, 10a and b) and cause difficulty in the phase unwrapping process, resulting in unstable elevations and large uncertainty of TRI DEMs over these regions.

5.5. Systematic error source of TRI DEM

The accuracy of TRI DEM can be influenced by many factors. Systematic errors are directly from TRI observation characteristics and operation settings, which include range accuracy, phase sensitivity, baseline accuracy, and view angle. Since the contribution of error sources to final DEM accuracy is neither linear, nor independent, following Strozzi et al. (2011) and from Eq. (5), the contribution of error source to the final DEM accuracy is listed as Eqs. (15) to (18) separately assuming only one error source exists at the same time.

$$d_{z\_r} = \frac{\lambda \varnothing}{2\pi b}\sigma_r \tag{15}$$

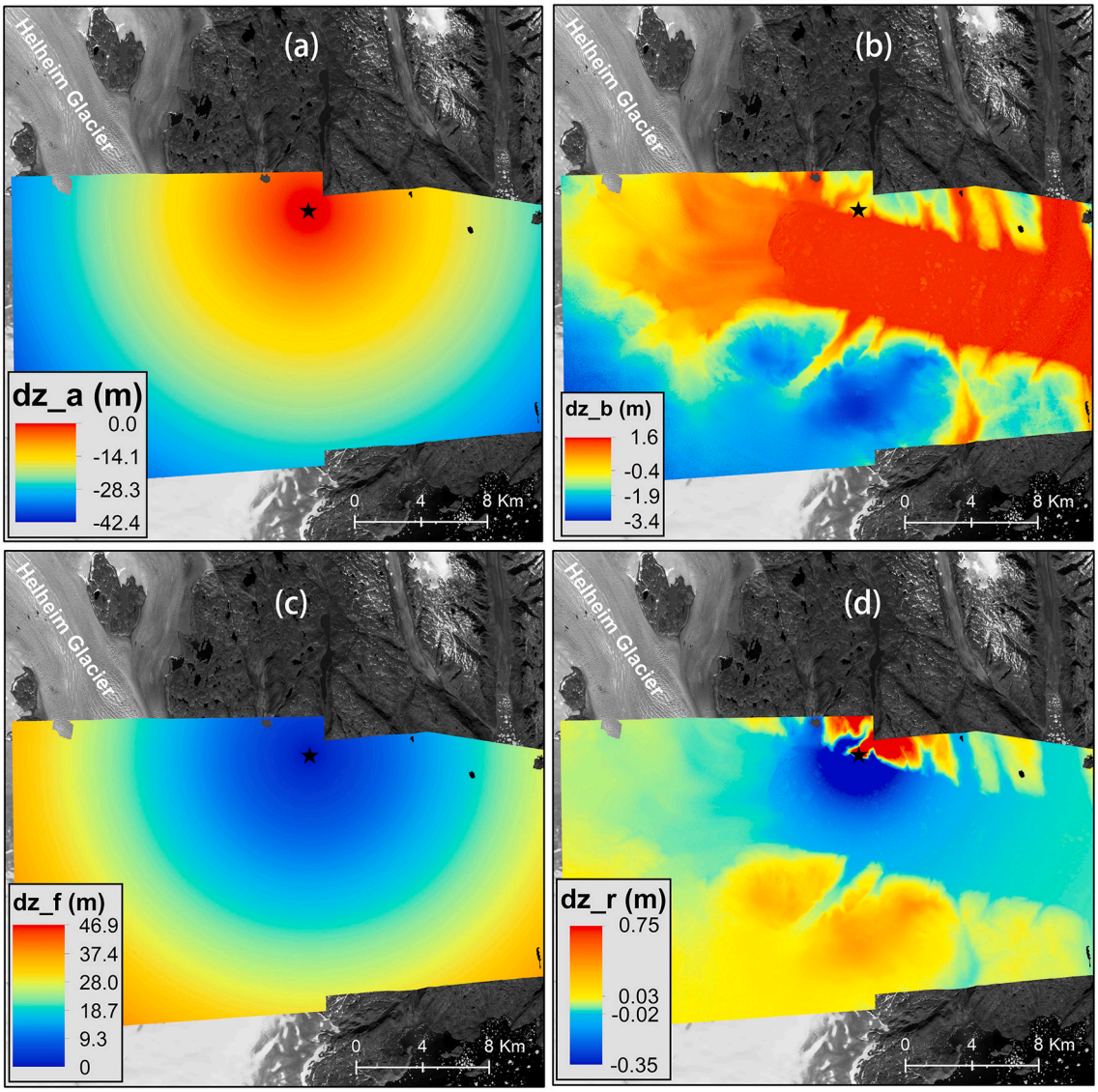

Fig. 10. DEM uncertainty generated from each different systematic error source of TRI. (a), (b), (c) and (d) stand for error source of final elevation from baseline angle, baseline, phase and range accuracy respectively. The black solid star indicates the location of TRI near Helheim Glacier. Components dz_r, dz_f, dz_b and dz_a indicate the contribution of TRI range, phase, baseline, and view angle accuracy to the final accuracy of the TRI DEM respectively. The occlusion of TRI view because of terrain undulation is not considered in these simulation results.

$$d_{z\_f} = \left(\frac{\lambda r_2}{2\pi b} - \frac{\lambda^2 \varnothing}{4\pi^2 b}\right)\sigma_{\varnothing} \tag{16}$$

$$d_{z\_b} = \left(\frac{1}{2} + \frac{\lambda^2 \varnothing^2}{8\pi^2 b^2} - \frac{\lambda r_2 \varnothing}{2\pi b^2}\right)\sigma_b \tag{17}$$

$$d_{z\_a} = -r_2 sin(\theta + \alpha)\sigma_{\alpha} \tag{18}$$

where σ_r, $\sigma_{\varnothing}$, σ_b and σ_{α} is the range accuracy, phase sensitivity, baseline accuracy and view angle bias respectively. d_{z_r} , d_{z_f}, d_{z_b} and d_{z_a} represent the TRI DEM uncertainty propagated from range, phase, baseline and view angle accuracy respectively.

The geolocation of TRI from GPS and the corrected ArcticDEM are taken to simulate the contribution of range accuracy ($\sigma_r = \pm 0.75\ m$), phase accuracy ($\sigma_{\varnothing} = \pm 10°$), baseline accuracy ($\sigma_b = \pm 0.1\ cm$), view angle accuracy ($\sigma_{\alpha} = \pm 0.1°$) respectively, as shown in Fig. 10.

The TRI DEM error propagation from the four error sources mentioned above are summarized as follows. TRI DEM error caused by view angle accuracy (dz_a) is located in [−42.4, 0] m, which is relatively large (Fig. 10 a). Fig. 10a also suggests that the error is almost linearly distributed with range which is owing to the similar view angle over most of the study area. Even a 0.1° view angle error tends to cause a large elevation error at far range, which is approximately 42.4 m. Proper leveling the TRI motor and making sure TRI frame perpendicular to flat surface before and during the deployment is key to eliminate this error. TRI DEM error caused by baseline accuracy (dz_b) is relatively small which is located in [−3.4, 1.6] m (Fig. 10b). TRI elevation is less affected by baseline accuracy as the equipment is delicately designed, but the spatial distribution of elevation error propagating from this is nonlinear with range and is highly correlated to topographic undulation. TRI DEM error caused by phase accuracy (dz_f) is located in [0, 46.9] m, the magnitude of which is similar to that from dz_a (Fig. 10 c). Fig. 10c also suggests the error is almost linearly distributed with range which is owing to the second term of Eq. (16) is close to zero. In the study area, a 10° phase accuracy will cause large elevation errors at far range, close to 46 m. TRI DEM error caused by range accuracy (dz_r) is located in [−0.35, 0.75] m, which is small (Fig. 10 d). Thus, TRI DEM is less affected by range uncertainty.

Fig. 7c shows a dominant and linear changing trend of elevation error of TRI DEM versus range which likely results from systematic error contribution from phase sensitivity and view angle bias. This linear trend can be further eliminated by applying more ground control points distributed at different ranges, like what has been conducted in Xie et al. (2019). In this study the linear trend has a slope of - 0.02 (Fig. 7c), which indicates the elevation from TRI would decrease by about 20 m if range increased by 1000 m. As the error propagation of phase sensitivity and view angle bias enlarges with range, multiple ground control points at different ranges should be selected to fit the variation trend of error, remove the error and increase the accuracy of TRI DEM.

The analysis of systematic error of TRI DEM has shown that the error source is neither independent to each other, nor linearly contributing to the final elevation error. Although the linear error of TRI DEM can be removed, the uncertainty (standard deviation) at different ranges as shown in Fig. 9a could not be reduced by this process. Besides of systematic error source mentioned above, some other errors may also contribute to final TRI DEM uncertainty. The view angle may change with wind and local atmospheric conditions, which may lead to uneven distribution of view angle accuracy over the study area. Discontinued topographic phase may cause larger uncertainty in phase unwrapping, resulting in worse phase accuracy in those specific regions. How to completely remove all errors propagated from view angle and phase accuracy is still challenging. Additionally, the TRI DEM is also influenced by baseline error and range accuracy, which is difficult to determine in this research. Although the error contribution from both is small, how to effectively remove their contribution to the final elevation uncertainty deserves more work.

5.6. Other error sources of TRI DEM

The ellipsoidal correction relies on an approximate method in Section 3.1 (Supplementary Fig. 1). However, this approximate correction does not degrade the TRI DEM accuracy, as the topographic variation is far smaller than the Earth's radius. The red dots in Fig. 7c indicate that the results from land surface with the same elevation with TRI center. Although the ellipsoidal correction has been applied to these points, the linear trend of elevation difference is remains for these points.

Another reason for poor accuracy of TRI DEM at far range may be related to coarser azimuth resolution at far range than at the near range. In Section 2.1, we mentioned that the azimuth resolution depends on the antenna pattern, which is dominated by the antenna length and waveguide geometry. The TRI antenna half-power beam width is 0.385 degrees, so the azimuth resolution at near range is smaller than the far range due the arc length formula (The azimuth resolution of TRI image at 1 km, 5 km,10 km and 15 km can be approximately 7.5 m, 37.5 m, 75.0 m, and 112.5 m, which degrades linearly with range). A coarser azimuth resolution degrades the accuracy of TRI DEM since the backscattered signal comes from a larger area at far range than at near range.

The third reason should be related to limited ground control points adopted in this study. Only one ground control point was used during phase unwrapping process. However, because of the error contribution of phase sensitivity enlarged with range, only one ground control point is not enough to show the linear trend of error propagation. Although in-situ ground control points are difficult to collect, especially in glacier surface, historical DEM data obtained within a short time interval to TRI observation can also provide effective ground control and potentially be used to improve the accuracy of TRI DEM. This finding is similar to what has been shown in Xie et al. (2019).

5.7. Improving TRI DEM by averaging

We investigate the improvement of TRI DEM due to averaging more by using 10, 20, 30, 40, 50 and 60 min observation periods (each pair with a time interval of 2 min). The amplitude of elevation variation in 60 min observation period is shown in Fig. 11a. Similar with Fig. 9a, the amplitude of elevation changes with range (Fig. 11b, and c) is calculated by averaging all effective samples at the same range first and then referencing the elevation anomaly from the 60 min TRI DEM as shown in Fig. 11b and c.

Since the ice flow velocity for Helheim Glacier is ~24 m/d (Voytenko et al., 2015a, 2015b), the maximum displacement of ice over one hour is close to 1 m. At the same time, ice mélange in the fjord would have moved vertically with the tide. In order to remove the influence of the changing signal from tide and ice motion, DEM difference from land surface which corresponds to rock outcrops and land ice (black box in Fig. 11a) is used to illustrate whether significant improvement can be achieved by using DEM averaged across multiple observations. Fig. 11b and c suggest that the improvement of TRI DEM by averaging longer observations (~1 h) can approach 0.5 to 1.2 m uncertainty at range of ~7 km to ~10 km and the improvement tends to increase linearly. This result indicates that TRI can provide stable and precise measurements over stable land surface. Fig. 11 also indicates that the DEM precision at far range and spatially disconnected region is poor, which may be over several tens of meters. Radar shadow and low coherence region tends to interrupt the interferogram resulting in large uncertainty in phase unwrapping and elevation inversion.

6. Conclusion

In this study, we introduced the correction of TRI DEMs to the WGS-84 ellipsoid and investigated various factors related to the accuracy and error sources of TRI DEMs, how much the accuracy of TRI DEMs can be

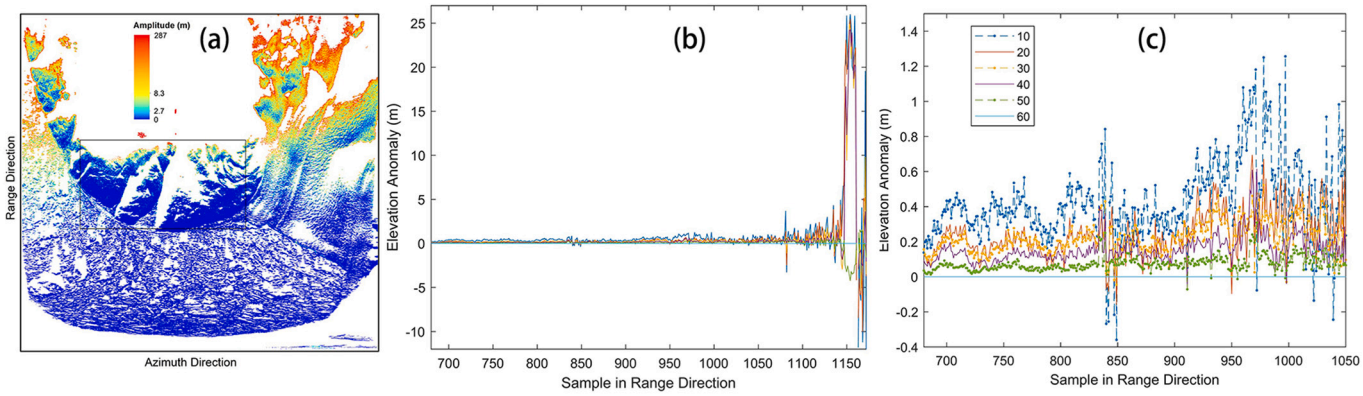

Fig. 11. (a) shows the changing amplitude of TRI DEMs generated from10, 20, 30, 40, 50 and 60 min period (the x and y axes stand for the azimuth and range respectively). The amplitude of elevation change for each pixel is calculated by subtracting the lowest elevation from the highest one. No ice mélange pixels in black box are taken for analysis in (b) and (c). (b) shows elevation difference along range for different TRI DEMs generated in 10, 20, 30, 40, 50 and 60 min. The elevation from 60 min is taken as reference to calculate the elevation anomaly. (c) enlarged range samples from 680 to 1050. Each sample corresponds to 10 m in range.

improved by stacking observations across time, relation of the accuracy with range, correlation coefficients and whether TRI DEM is comparable with historical DEMs from remote sensing techniques, such as photogrammetry.

TRI DEMs have relatively stable performance when unwrapped with an interferometric correlation coefficient greater than 0.6. The uncertainty of elevation at near range (less than 9.8 km) is <5 m. However, the uncertainty gets worse when range is between 9.8 and 18.6 km. This study also shows that increasing the correlation coefficient threshold before phase unwrapping (e.g. from 0.6 to 0.8) neither decreases the uncertainty (standard deviation) of TRI DEM, nor excludes large uncertainty elevation pixels larger than 50 m. Therefore, in TRI DEM generation, if phase unwrapping is not an issue, a higher correlation coefficient threshold (i.e., >0.8) is not recommended. This study also suggests that averaging TRI DEMs over a longer-time period, such as one hour, can help to improve the accuracy at short range (less than 9.3 km) almost linearly. However, this improvement is limited to ~0.5 m at range of ~9.0 km and no obvious improvement is detected farther.

We compared the TRI DEM over Helheim Glacier with the accurate ArcticDEM. This comparison also indicates that the TRI DEM is less accurate at far range. As such, caution should be taken to investigate glacier changes at far range, especially when comparing TRI DEMs with other historical DEMs. The systematic characteristics of TRI such as phase and view angle accuracy contribute larger errors to elevation uncertainty than that propagated from base line and range accuracy. However, the error contribution from phase and view angle accuracy is almost linear distributed with ranges at space, can be effectively fitted and eliminated by adopting more ground control points at different ranges. In this study, degraded azimuth resolution at far range and the phase unwrapping difficulties caused by discontinuous topographic phase at far range may be primarily related to the large error found in this comparison.

Regions at near range with good spatial phase continuity should be the primary focus of TRI observations for glaciological researches. Although systematic error sources cannot be avoided in the TRI DEMs, proper image processing, such as image rotation is required to obtain the best horizontal position of the TRI DEMs to make it comparable with other DEMs. TRI DEMs do not have high accuracy at far range, but in near range (less than 9.8 km), they are relative stable and have low uncertainty (less than 5 m) making them suitable for detecting elevation changes of glaciers in polar regions by combing them with other remote sensing observations.

Credit author statement

Xianwei Wang collected the data, finished the data processing, drew all the figures, and prepared a manuscript and the revision of this study. Denis Voytenko contributed to data processing by providing some python code and revision of the manuscript. David M. Holland contributed to data collection and revision of this manuscript. All authors discussed the method, results and major findings of this study.

Declaration of Competing Interest

The authors declare that they have no known competing financial interests or personal relationships that could have appeared to influence the work reported in this paper.

Acknowledgement

We acknowledge Denise Holland from Center for Global Sea Level Change, New York University Abu Dhabi for organizing the field logistics. This research was supported by the Center for Global Sea Level Change (CSLC) of NYU Abu Dhabi Research Institute (G1204), the National Science Foundation (ARC-1304137) of the USA, NASA Oceans Melting Greenland to NYU (NNX15AD55G) and Advanced Polar Science Institute of Shanghai (APSIS). We are grateful to United States Geological Survey (USGS) for free use of Landsat images, to the National Snow and Ice Data Center (NSIDC) for free use of ICESat/GLAS and ICESat-2/ATLAS data. The ArcticDEM is provided by the Polar Geospatial Center under NSF-OPP awards 1043681 and 1559691.

Appendix A. Supplementary data

Supplementary data to this article can be found online at https://doi.org/10.1016/j.rse.2021.112759.

References

Brown, C.G., Sarabandi, K., Pierce, L.E., 2005. Validation of the shuttle radar topography mission height data. IEEE Trans. Geosci. Remote Sens. 43 (8), 1707–1715.
Brunt, K.M., Neumann, T.A., Smith, B.E., 2019. Assessment of ICESat-2 ice sheet surface heights, based on comparisons over the interior of the Antarctic ice sheet. Geophys. Res. Lett. 46 (22), 13072–13078.
Burton-Johnson, A., Black, M., Fretwell, P., Kaluza-Gilbert, J., 2016. An automated methodology for differentiating rock from snow, clouds and sea in Antarctica from Landsat 8 imagery: a new rock outcrop map and area estimation for the entire Antarctic continent. Cryosphere 10, 1665–1677.
Caduff, R., Schlunegger, F., Kos, A., Wiesmann, A., 2015. A review of terrestrial radar interferometry for measuring surface change in the geosciences. Earth Surf. Process. Landf. 40 (2), 208–228.
Cassotto, R., Fahnestock, M., Amundson, J.M., Truffer, M., Joughin, I., 2015. Seasonal and interannual variations in ice melange and its impact on terminus stability, Jakobshavn Isbræ, Greenland. J. Glaciol. 61 (225), 76–88.

Cassotto, R., Fahnestock, M., Amundson, J.M., Truffer, M., Boettcher, M.S., de La Peña, S., Howat, I., 2019. Non-linear glacier response to calving events, Jakobshavn Isbræ, Greenland. J. Glaciol. 65 (249), 39–54.
Cassotto, R.K., Burton, J.C., Amundson, J.M., Fahnestock, M.A., Truffer, M., 2021. Granular decoherence precedes ice mélange failure and glacier calving at Jakobshavn Isbræ. Nat. Geosci. 14 (6), 417–422.
Choi, H., Bindschadler, R., 2004. Cloud detection in Landsat imagery of ice sheets using shadow matching technique and automatic normalized difference snow index threshold value decision. Remote Sens. Environ. 91 (2), 237–242.
Cox, P.M., Betts, R.A., Jones, C.D., Spall, S.A., Totterdell, I.J., 2000. Acceleration of global warming due to carbon-cycle feedbacks in a coupled climate model. Nature. 408 (6809), 184–187.
Crawford, C.J., Manson, S.M., Bauer, M.E., Hall, D.K., 2013. Multitemporal snow cover mapping in mountainous terrain for Landsat climate data record development. Remote Sens. Environ. 135, 224–233.
Dai, C.l., Durand, M., Howat, I.M., Altenau, E.H., Pavelsky, T.M., 2018. Estimating river surface elevation from ArcticDEM. Geophys. Res. Lett. 45 (7), 3107–3114.
Dall, J., Madsen, S.N., Keller, K., Forsberg, R., 2001. Topography and penetration of the Greenland ice sheet measured with airborne SAR interferometry. Geophys. Res. Lett. 28 (9), 1703–1706.
Dixon, T.H., Voytenko, D., Lembke, C., de La Peña, S., Howat, I., Gourmelen, N., Werner, C., Oddsson, B., 2012. Emerging technology monitors ice-sea interface at outlet glaciers. EOS Trans. Am. Geophys. Union 93 (48), 497–498.
Dozier, J., 1989. Spectral signature of alpine snow cover from the Landsat thematic mapper. Remote Sens. Environ. 28 (1), 9–22.
E, D., Shen, Q., Xu, Y., Chen, G., 2009. High-accuracy topographical information extraction based on fusion of ASTER stereo-data and ICESat/GLAS data in Antarctica. Sci. China Ser. D Earth Sci. 52 (5), 714–722.
Everett, A., Murray, T., Selmes, N., Holland, D., Reeve, D.E., 2021. The impacts of a subglacial discharge plume on calving, submarine melting, and Mélange Mass Loss at Helheim Glacier, South East Greenland. J. Geophys. Res. Earth Surf. 126 (3), e2020JF005910.
Fricker, H.A., Borsa, A., Minster, B., Carabajal, C., Quinn, K., Bills, B., 2005. Assessment of ICESat performance at the Salar de Uyuni, Bolivia. Geophys. Res. Lett. 32 (21).
Gelautz, M., Paillou, P., Chen, C.W., Zebker, H.A., 2003. Radar stereo-and interferometry-derived digital elevation models: comparison and combination using Radarsat and ERS-2 imagery. Int. J. Remote Sens. 24 (24), 5243–5264.
Goldstein, R.M., Werner, C.L., 1998. Radar interferogram filtering for geophysical applications. Geophys. Res. Lett. 25 (21), 4035–4038.
Gorokhovich, Y., Voustianiouk, A., 2006. Accuracy assessment of the processed SRTM-based elevation data by CGIAR using field data from USA and Thailand and its relation to the terrain characteristics. Remote Sens. Environ. 104 (4), 409–415.
Goward, S.N., Masek, J.G., Williams, D.L., Irons, J.R., Thompson, R.J., 2001. The Landsat 7 mission: terrestrial research and applications for the 21st century. Remote Sens. Environ. 78 (1–2), 3–12.
Holland, D.M., Thomas, R.H., Young, B.D., Ribergaard, M.H., Lyberth, B., 2008. Acceleration of Jakobshavn Isbræ triggered by warm subsurface ocean waters. Nat. Geosci. 1 (10), 659–664.
Holland, D.M., Voytenko, D., Christianson, K., Dixon, T.H., Mel, M.J., Parizek, B.R., Vanková, I., 2016. An intensive observation of calving at Helheim Glacier, East Greenland. Oceanography. 29 (4), 46–61.
Howat, I.M., Joughin, I., Tulaczyk, S., Gogineni, S., 2005. Rapid retreat and acceleration of Helheim glacier, East Greenland. Geophys. Res. Lett. 32 (22).
Howat, I.M., Negrete, A., Smith, B.E., 2014. The Greenland ice mapping project (GIMP) land classification and surface elevation datasets. Cryosphere. 8, 1509–1518. https://doi.org/10.5194/tc-8-1509-2014.
Howat, I.M., Porter, C., Smith, B.E., Noh, M.J., Morin, P., 2019. The reference elevation model of Antarctica. Cryosphere. 13 (2), 665–674.
Hui, F., Cheng, X., Liu, Y., Zhang, Y., Ye, Y., Wang, X., Li, Z., Wang, K., Zhan, Z., Guo, J., Huang, H., 2013. An improved landsat image mosaic of Antarctica. Sci. China Earth Sci. 56 (1), 1–12.
Joughin, I., Alley, R.B., 2011. Stability of the West Antarctic ice sheet in a warming world. Nat. Geosci. 4 (8), 506–513.
Joughin, I., Shean, D.E., Smith, B.E., Floricioiu, D., 2020. A decade of variability on Jakobshavn Isbræ: ocean temperatures pace speed through influence on mélange rigidity. Cryosphere. 14 (1), 211.
Kehrl, L.M., Joughin, I., Shean, D.E., Floricioiu, D., Krieger, L., 2017. Seasonal and interannual variabilities in terminus position, glacier velocity, and surface elevation at Helheim and Kangerlussuaq glaciers from 2008 to 2016. J. Geophys. Res. Earth Surf. 122 (9), 1635–1652.
Khan, S.A., Bjørk, A.A., Bamber, J.L., Morlighem, M., Bevis, M., Kjær, K.H., Mouginot, J., Løkkegaard, A., Holland, D.M., Aschwanden, A., Zhang, B., 2020. Centennial response of Greenland's three largest outlet glaciers. Nat. Commun. 11 (1), 1–9.
Krabill, W.B., Abdalati, W., Frederick, E.B., Manizade, S.S., Martin, C.F., Sonntag, J.G., Yungel, J.G., 2002. Aircraft laser altimetry measurement of elevation changes of the Greenland ice sheet: technique and accuracy assessment. J. Geodyn. 34 (3-4), 357–376.
Lüthi, M.P., Vieli, A., 2016. Multi-method observation and analysis of a tsunami caused by glacier calving. Cryosphere 10 (3), 995–1002.
Markus, T., Neumann, T., Martino, A., Abdalati, W., Brunt, K., Csatho, B., Farrell, S., Fricker, H., Gardner, A., Harding, D., Jasinski, M., 2017. The ice, cloud, and land elevation Satellite-2 (ICESat-2): science requirements, concept, and implementation. Remote Sens. Environ. 190, 260–273.
Nitti, D.O., Bovenga, F., Nutricato, R., Intini, F., Chiaradia, M.T., 2013. On the use of COSMO/SkyMed data and weather models for interferometric DEM generation. Eur. J. Remote Sens. 46 (1), 250–271.
Noferini, L., Pieraccini, M., Mecatti, D., Macaluso, G., Luzi, G., Atzeni, C., 2007. DEM by ground-based SAR interferometry. IEEE Geosci. Remote Sens. Lett. 4 (4), 659–663.
Noh, M.J., Howat, I.M., 2015. Automated stereo-photogrammetric DEM generation at high latitudes: Surface Extraction with TIN-based Search-space Minimization (SETSM) validation and demonstration over glaciated regions. GISci. Remote Sens. 52 (2), 198–217.
Oppenheimer, Michael, 1998. Global warming and the stability of the West Antarctic Ice Sheet. Nature. 393 (6683), 325–332.
Paolo, F.S., Fricker, H.A., Padman, L., 2015. Volume loss from Antarctic ice shelves is accelerating. Science. 348 (6232), 327–331.
Paul, F., 2008. Calculation of glacier elevation changes with SRTM: is there an elevation-dependent bias? J. Glaciol. 54 (188), 945–946.
Peters, I.R., Amundson, J.M., Cassotto, R., Fahnestock, M., Darnell, K.N., Truffer, M., Zhang, W.W., 2015. Dynamic jamming of iceberg-choked fjords. Geophys. Res. Lett. 42 (4), 1122–1129.
Pieraccini, M., Miccinesi, L., 2019. Ground-based radar interferometry: a bibliographic review. Remote Sens. 11 (9), 1029.
Porter, Claire, Morin, Paul, Howat, Ian, Noh, Myoung-Jon, Bates, Brian, Peterman, Kenneth, Keesey, Scott, Schlenk, Matthew, Gardiner, Judith, Tomko, Karen, Willis, Michael, Kelleher, Cole, Cloutier, Michael, Husby, Eric, Foga, Steven, Nakamura, Hitomi, Platson, Melisa, Wethington, Michael, Jr, Williamson, Cathleen, Bauer, Gregory, Enos, Jeremy, Arnold, Galen, Kramer, William, Becker, Peter, Doshi, Abhijit, D'Souza, Cristelle, Cummens, Pat, Laurier, Fabien, Bojesen, Mikkel, 2018. ArcticDEM, V1. Harvard Dataverse. https://doi.org/10.7910/DVN/OHHUKH [Accessed on April 10, 2020].
Pritchard, H., Ligtenberg, S.R., Fricker, H.A., Vaughan, D.G., van den Broeke, M.R., Padman, L., 2012. Antarctic ice-sheet loss driven by basal melting of ice shelves. Nature. 484 (7395), 502–505.
Rignot, E., Velicogna, I., van den Broeke, M.R., Monaghan, A., Lenaerts, J.T., 2011. Acceleration of the contribution of the Greenland and Antarctic ice sheets to sea level rise. Geophys. Res. Lett. 38 (5).
Rizzoli, P., Martone, M., Gonzalez, C., Wecklich, C., Tridon, D.B., Bräutigam, B., Bachmann, M., Schulze, D., Fritz, T., Huber, M., Wessel, B., 2017. Generation and performance assessment of the global TanDEM-X digital elevation model. ISPRS J. Photogramm. Remote Sens. 132.119–139.
Rodriguez, E., Morris, C.S., Belz, J.E., 2006. A global assessment of the SRTM performance. Photogramm. Eng. Remote. Sens. 72 (3), 249–260.
Sandwell, D.T., Sichoix, L., 2000. Topographic phase recovery from stacked ERS interferometry and a low-resolution digital elevation model. J. Geophys. Res. Solid Earth 105 (B12), 28211–28222.
Shean, D.E., Joughin, I.R., Dutrieux, P., Smith, B.E., Berthier, E., 2019. Ice shelf basal melt rates from a high-resolution digital elevation model (DEM) record for Pine Island glacier, Antarctica. Cryosphere. 13 (10), 2633–2656.
Shepherd, A., Ivins, E., Rignot, E., Smith, B., Van Den Broeke, M., Velicogna, I., Whitehouse, P., Briggs, K., Joughin, I., Krinner, G., Nowicki, S., 2018. Mass balance of the Antarctic Ice Sheet from 1992 to 2017. Nature. 558, 219–222.
Shuman, C.A., Zwally, H.J., Schutz, B.E., Brenner, A.C., DiMarzio, J.P., Suchdeo, V.P., Fricker, H.A., 2006. ICESat Antarctic elevation data: preliminary precision and accuracy assessment. Geophys. Res. Lett. 33 (7).
Smith, B., Fricker, H.A., Holschuh, N., Gardner, A.S., Adusumilli, S., Brunt, K.M., Csatho, B., Harbeck, K., Huth, A., Neumann, T., Nilsson, J., 2019. Land ice height-retrieval algorithm for NASA's ICESat-2 photon-counting laser altimeter. Remote Sens. Environ. 233 (111352).
Smith, B., Fricker, H.A., Gardner, A.S., Medley, B., Nilsson, J., Paolo, F.S., Zwally, H.J., 2020. Pervasive ice sheet mass loss reflects competing ocean and atmosphere processes. Science 368 (6496), 1239–1242.
Strozzi, T., Werner, C., Wiesmann, A., Wegmuller, U., 2011. Topography mapping with a portable real-aperture radar interferometer. IEEE Geosci. Remote Sens. Lett. 9 (2), 277–281.
Tachikawa, T., Kaku, M., Iwasaki, A., Gesch, D.B., Oimoen, M.J., Zhang, Z., Danielson, J. J., Krieger, T., Curtis, B., Haase, J., Abrams, M., 2011. ASTER Global Digital Elevation Model Version 2-Summary of Validation Results. NASA.
Tadono, T., Ishida, H., Oda, F., Naito, S., Minakawa, K., Iwamoto, H., 2014. Precise global DEM generation by ALOS PRISM. ISPRS Annals of the Photogrammetry, Remote Sensing and Spatial Information Sciences 2 (4), 71.
Takaku, J., Tadono, T., Tsutsui, K., Ichikawa, M., 2018, July. Quality improvements of 'AW3D' global DSM derived from ALOS prism. In: IGARSS 2018-2018 IEEE International Geoscience and Remote Sensing Symposium. IEEE, pp. 1612–1615.
Telling, J.W., Glennie, C., Fountain, A.G., Finnegan, D.C., 2017. Analyzing glacier surface motion using LiDAR data. Remote Sens. 9 (3), 283.
Velicogna, I., 2009. Increasing rates of ice mass loss from the Greenland and Antarctic ice sheets revealed by GRACE. Geophys. Res. Lett. 36 (19).
Voytenko, D., Dixon, T.H., Werner, C., Gourmelen, N., Howat, I.M., Tinder, P.C., Hooper, A., 2012, July. Monitoring a glacier in southeastern Iceland with the portable terrestrial radar interferometer. In: 2012 IEEE International Geoscience and Remote Sensing Symposium. IEEE, pp. 3230–3232.
Voytenko, D., Stern, A., Holland, D.M., Dixon, T.H., Christianson, K., Walker, R.T., 2015a. Tidally driven ice speed variation at Helheim glacier, Greenland, observed with terrestrial radar interferometry. J. Glaciol. 61 (226), 301–308.
Voytenko, D., Dixon, T.H., Howat, I.M., Gourmelen, N., Lembke, C., Werner, C.L., De La Peña, S., Oddsson, B., 2015b. Multi-year observations of Breiðamerkurjökull, a marine-terminating glacier in southeastern Iceland, using terrestrial radar interferometry. J. Glaciol. 61 (225), 42–54.
Voytenko, D., Dixon, T.H., Holland, D.M., Cassotto, R., Howat, I.M., Fahnestock, M.A., Truffer, M., De la Pena, S., 2017. Acquisition of a 3 min, two-dimensional glacier velocity field with terrestrial radar interferometry. J. Glaciol. 63 (240), 629–636.

Walter, F., Gräff, D., Lindner, F., Paitz, P., Köpfli, M., Chmiel, M., Fichtner, A., 2020. Distributed acoustic sensing of microseismic sources and wave propagation in glaciated terrain. Nat. Commun. 11 (1), 1–10.
Wang, X., Holland, D.M., 2018. A method to calculate elevation-change rate of Jakobshavn Isbrae using operation IceBridge airborne topographic mapper data. IEEE Geosci. Remote Sens. Lett. 15 (7), 981–985.
Wang, X., Cheng, X., Gong, P., Huang, H., Li, Z., Li, X., 2011. Earth science applications of ICESat/GLAS: a review. Int. J. Remote Sens. 32 (23), 8837–8864.
Wang, X., Cheng, X., Huang, H., Li, Z., 2013. DEM production for dome-a combining GPS and GLAS data. Yaogan Xuebao- J. Remote Sens. 17 (2), 439–451.
Wang, X., Holland, D.M., Cheng, X., Gong, P., 2016. Grounding and calving cycle of Mertz ice tongue revealed by shallow Mertz Bank. Cryosphere. 10 (5), 2043–2056.
Wang, X., Holland, D.M., Gudmundsson, G.H., 2018. Accurate coastal DEM generation by merging ASTER GDEM and ICESat/GLAS data over Mertz Glacier, Antarctica. Remote Sens. Environ. 206.218–230.
Wegmüller, U., Santoro, M., Werner, C., Strozzi, T., Wiesmann, A., Lengert, W., 2009. DEM generation using ERS–ENVISAT interferometry. J. Appl. Geophys. 69 (1), 51–58.
Werner, C., Wegmüller, U., Strozzi, T., Wiesmann, A., 2002, June. Processing strategies for phase unwrapping for INSAR applications. In: In Proceedings of the European Conference on Synthetic Aperture Radar EUSAR.
Werner, C., Strozzi, T., Wiesmann, A., Wegmuller, U., 2008, July. A real-aperture radar for ground-based differential interferometry. In: IGARSS 2008-2008 IEEE International Geoscience and Remote Sensing Symposium, Vol. 3. IEEE, p. III-210.
Werner, C., Strozzi, T., Wiesmann, A., Wegmuller, U., 2009. A ground-based real-aperture radar instrument for differential interferometry. In: 2009 IEEE Radar Conference. IEEE, pp. 1–4.
Wood, M., Rignot, E., Fenty, I., An, L., Bjørk, A., van den Broeke, M., Zhang, H., 2021. Ocean forcing drives glacier retreat in Greenland. Sci. Adv. 7 (1), eaba7282.
Xie, S., Dixon, T.H., Voytenko, D., Holland, D.M., Holland, D., Zheng, T., 2016. Precursor motion to iceberg calving at Jakobshavn Isbræ, Greenland, observed with terrestrial radar interferometry. J. Glaciol. 62 (236), 1134–1142.
Xie, S., Dixon, T.H., Voytenko, D., Deng, F., Holland, D.M., 2018. Grounding line migration through the calving season at Jakobshavn Isbræ, Greenland, observed with terrestrial radar interferometry. Cryosphere. 12 (4), 1387.
Xie, S., Dixon, T.H., Holland, D.M., Voytenko, D., Vaňková, I., 2019. Rapid iceberg calving following removal of tightly packed pro-glacial mélange. Nat. Commun. 10 (1), 1–15.
Yu, J.H., Ge, L., Li, X., 2014. Radargrammetry for digital elevation model generation using Envisat reprocessed image and simulation image. IEEE Geosci. Remote Sens. Lett. 11 (9), 1589–1593.
Zebker, H.A., Goldstein, R.M., 1986. Topographic mapping from interferometric synthetic aperture radar observations. J. Geophys. Res. Solid Earth 91 (B5), 4993–4999.
Zink, M., Bachmann, M., Brautigam, B., Fritz, T., Hajnsek, I., Moreira, A., Wessel, B., Krieger, G., 2014. TanDEM-X: the new global DEM takes shape. IEEE Geosci. Remote Sens. Mag. 2 (2), 8–23.
Zwally, H.J., Schutz, B., Abdalati, W., Abshire, J., Bentley, C., Brenner, A., Thomas, R., 2002. ICESat's laser measurements of polar ice, atmosphere, ocean, and land. J. Geodyn. 34 (3-4), 405–445.